A modern scleractinian coral with a two-component calcite–aragonite skeleton

Jarosław Stolarski[a,1], Ismael Coronado[b], Jack G. Murphy[c], Marcelo V. Kitahara[d,e], Katarzyna Janiszewska[a], Maciej Mazur[f], Anne M. Gothmann[g,h], Anne-Sophie Bouvier[i], Johanna Marin-Carbonne[i], Michelle L. Taylor[j], Andrea M. Quattrini[k,l], Catherine S. McFadden[l], John A. Higgins[c], Laura F. Robinson[m], and Anders Meibom[i,n]

[a]Institute of Paleobiology, Polish Academy of Sciences, PL-00-818 Warsaw, Poland; [b]Faculty of Biological and Environmental Sciences, University of Leon, 24171 Leon, Spain; [c]Department of Geosciences, Princeton University, Princeton, NJ 08544; [d]Marine Science Department, Federal University of São Paulo, 11070-100 Santos (SP), Brazil; [e]Centre for Marine Biology, University of São Paulo, 11612-109 São Sebastião (SP), Brazil; [f]Department of Chemistry, University of Warsaw, PL-02-093 Warsaw, Poland; [g]Department of Environmental Studies, St. Olaf College, Northfield, MN 55057; [h]Department of Physics, St. Olaf College, Northfield, MN 55057; [i]Center for Advanced Surface Analysis, Institute of Earth Sciences, Université de Lausanne, CH-1015 Lausanne, Switzerland; [j]School of Life Sciences, University of Essex, Wivenhoe Park, CO4 3SQ Colchester, United Kingdom; [k]Department of Invertebrate Zoology, Smithsonian Institution, Washington, DC 20560-0163; [l]Department of Biology, Harvey Mudd College, Claremont, CA 91711; [m]School of Earth Sciences, University of Bristol, BS8 1RJ Clifton, United Kingdom; and [n]Laboratory for Biological Geochemistry, School of Architecture, Civil and Environmental Engineering, Ecole Polytechnique Fédérale de Lausanne, CH-1015 Lausanne, Switzerland

Edited by Paul G. Falkowski, Rutgers University, New Brunswick, NJ, and approved November 4, 2020 (received for review June 29, 2020)

One of the most conserved traits in the evolution of biomineralizing organisms is the taxon-specific selection of skeletal minerals. All modern scleractinian corals are thought to produce skeletons exclusively of the calcium-carbonate polymorph aragonite. Despite strong fluctuations in ocean chemistry (notably the Mg/Ca ratio), this feature is believed to be conserved throughout the coral fossil record, spanning more than 240 million years. Only one example, the Cretaceous scleractinian coral *Coelosmilia* (ca. 70 to 65 Ma), is thought to have produced a calcitic skeleton. Here, we report that the modern asymbiotic scleractinian coral *Paraconotrochus antarcticus* living in the Southern Ocean forms a two-component carbonate skeleton, with an inner structure made of high-Mg calcite and an outer structure composed of aragonite. *P. antarcticus* and Cretaceous *Coelosmilia* skeletons share a unique microstructure indicating a close phylogenetic relationship, consistent with the early divergence of *P. antarcticus* within the Vacatina (i.e., Robusta) clade, estimated to have occurred in the Mesozoic (ca. 116 Mya). Scleractinian corals thus join the group of marine organisms capable of forming bimineralic structures, which requires a highly controlled biomineralization mechanism; this capability dates back at least 100 My. Due to its relatively prolonged isolation, the Southern Ocean stands out as a repository for extant marine organisms with ancient traits.

biomineralization | calcium carbonate | scleractinian corals | evolution | Southern Ocean

The ability to form a calcium carbonate skeleton represents an evolutionary innovation of major importance that dates back to the onset of the Phanerozoic (ca. 540 Ma) (1). Since that time, multiple groups of marine metazoans became highly efficient reef builders, creating the structural foundation for the richest and most biodiverse ecosystems in the ocean (2). In our modern ocean, carbonate reef building is dominated by scleractinian corals, which produce ~10^{12} kg of skeleton carbonate every year (3). Based on available empirical evidence, it is widely accepted that pristine skeletons of modern scleractinians, grown in natural environments, consist exclusively of the carbonate polymorph aragonite, which is metastable at ambient conditions typical of the Earth's surface.

In vitro experiments under ambient temperatures show that abiotic precipitation of calcium carbonate polymorphs from seawater is controlled primarily by the Mg/Ca ratio (4). With present-day ionic strengths and atmospheric CO_2 concentration (pH ca. 8), the seawater Mg/Ca ratio (today 5.2 mol/mol) separates two regimes of inorganic carbonate polymorph precipitation: the regime of low-magnesium calcite (LMC) at Mg/Ca < 2 mol/mol ("calcitic seas") and the regime of aragonite and/or high-Mg calcite (HMC) precipitation at Mg/Ca > 2 mol/mol ("aragonitic seas") (5, 6). During the mid-Cretaceous, the Mg/Ca ratio is thought to have been well below 2 mol/mol (7, 8), creating conditions conducive to calcite precipitation. Despite that, only one scleractinian coral, *Coelosmilia* from Upper Cretaceous chalk deposits, has, to date, been documented to have a bona fide primary calcitic skeleton (9). This observation is consistent with biomineralizing organisms exerting stronger control over polymorph selection than a simple inorganic precipitation process.

Coral skeletal microstructural patterns are highly conserved through evolution and have often been used to elucidate phylogenetic relationships in the absence of genetic information (10). Corals exhibiting similar microstructure very likely share a similar origin. Indeed, the biomineralization process has proven to be robust enough to withstand dramatic environmental changes throughout geological time, including substantial changes in seawater chemistry (11, 12).

In this context, we report the discovery that the extant, deep-sea, solitary, scleractinian coral *Paraconotrochus antarcticus*, which is ubiquitous in the Southern Ocean around Antarctica

Significance

Until now, all of the ca. 1,800 known modern scleractinian coral species were thought to produce skeletons exclusively of aragonite. Asymbiotic *Paraconotrochus antarcticus* living in the Southern Ocean is the first example of an extant scleractinian that forms a two-component carbonate skeleton, with an inner structure made of high-Mg calcite and an outer structure composed of aragonite. This discovery adds support to the notion that the coral skeletal formation process is strongly biologically controlled. Mitophylogenomic analysis shows that *P. antarcticus* represents an ancient scleractinian clade, suggesting that skeletal mineralogy/polymorph of a taxon, once established, is a trait conserved throughout the evolution of that clade.

Author contributions: J.S. designed research; J.S., I.C., J.G.M., M.V.K., K.J., M.M., A.-S.B., and J.M.-C. performed research; J.S., I.C., J.G.M., M.V.K., K.J., M.M., A.M.G., A.-S.B., J.M.-C., M.L.T., A.M.Q., C.S.M., J.A.H., L.F.R., and A.M. analyzed data; and J.S., I.C., J.G.M., M.V.K., and A.M. wrote the paper.

The authors declare no competing interest.

This article is a PNAS Direct Submission.

[1]To whom correspondence may be addressed. Email: stolacy@twarda.pan.pl.

This article contains supporting information online at https://www.pnas.org/lookup/suppl/doi:10.1073/pnas.2013316117/-/DCSupplemental.

Published December 15, 2020.

(13) at depths between 50 and 700 m and at temperatures between ca. 0.5 and 3 °C, forms a two-component calcite–aragonite skeleton with microstructural features very similar to the Cretaceous *Coelosmilia* (Fig. 1 and *SI Appendix*, Fig. S1).

Results

The samples of *P. antarcticus* studied here include both bare skeletons and specimens collected alive, obtained from material dredged from the Weddell, Ross, and Cooperation seas, respectively (*SI Appendix*, Fig. S2 and Table S1). The skeleton of *P. antarcticus* is shaped like a regular cone, which is a few centimeters in both diameter and height (Fig. 1 *A* and *B* and *SI Appendix*, Fig. S1 *A* and *B*). Its septa are hexamerally arranged in five cycles, and the central portion of the calice is occupied by labyrinthine projections (so-called columella).

In transversal cuts ($n = 31$), all examined *P. antarcticus* consistently revealed a distinct boundary between two main skeletal regions, hereafter referred to as the inner and outer skeleton (Fig. 1 *E*, *F*, and *H–J*). The inner skeleton is relatively narrow (ca. 50 to 100 μm thick) and forms the central parts of the septa and wall (Fig. 1 *E* and *H–J*). This inner skeleton is also observable at the distalmost (upper) growth front of the calice, where it is deposited quasi-contemporaneously with the outer skeleton (Fig. 1 *C* and *D*). Microstructurally, the inner skeleton consists of rapid accretion deposits (RADs; ca. 10 μm in diameter, also referred to as "centers of calcification") that define the central axis, and "fibrous" skeleton, or thickening deposits (TDs) ca. 20 to 30 μm thick, which consist of relatively broad ca. 10 μm bundles of fibers, completely transparent in transmitted light and flanking the RAD region (Fig. 2 *A* and *B*).

A sharp crystallographic boundary delineates the transition from the inner skeleton to the outer skeleton (Fig. 2 *F–H*). In those regions where the outer skeleton is in direct contact with the inner skeleton, the former typically consists of long (often > 100 μm) and relatively narrow (ca. 5 μm) bundles of crystal fibers (Fig. 2*G*). However, as the outer skeleton continues to form beyond the inner skeleton, it consists of the same two classical microstructural components (i.e., RADs overgrown by fibrous TDs, such as in Fig. 2*J* and *SI Appendix*, Figs. S3*B*, S5*C*, and S7 *E* and *F*). In contrast to the majority of other modern scleractinians, but in close structural analogy with Cretaceous *Coelosmilia*, the outer skeleton is gradually covered with a third carbonate structure that progressively infills the entire lumen of the calice bottom-up (*SI Appendix*, Figs. S1, S3–S6, and S9 *A* and *B*). All of these skeletal regions and components exhibit the nanoparticulate texture characteristic of biogenic minerals (14) when observed by scanning electron microscopy (SEM) and atomic force microscopy (AFM) (Fig. 2 *C–E*).

However, the observation of different calcium-carbonate polymorph compositions between the inner (calcite) and outer (aragonite) skeletons sets *P. antarcticus* apart from all other living scleractinian corals. The calcitic mineralogy of the inner skeleton is unequivocally demonstrated by both electron backscatter diffraction and Raman spectroscopy imaging of thin sections (Figs. 1*G* and 2*J* and *SI Appendix*, Fig. S10). The density difference between calcite and aragonite (2.65 to 2.71 g/cm^{-3} versus 2.94 g/cm^{-3}) makes these polymorphs distinguishable with high-resolution three-dimensional (3D) tomography, which revealed that the calcitic inner skeleton is a corrugated (and occasionally perforated/discontinuous) structure forming the central plane of the septa and wall (Fig. 1 *E* and *F*). Both 3D tomography and serial thin sectioning showed that the inner calcitic skeleton is usually present throughout the skeletal ontogeny (*SI Appendix*, Figs. S3–S6), although some specimens exhibited discontinuities in the development of the inner skeletal structure, typically accompanied by concentrically grown deposits (*SI Appendix*, Figs. S7 and S8). As expected, there is a sharp difference in chemical composition between the calcitic and aragonitic regions (Fig. 2 *L* and *M*). The calcitic inner skeleton is depleted in Sr and Na and enriched in Mg, averaging ca. 11 mole percent (mol%) of $MgCO_3$ and thus compositionally HMC, which is consistent with the observed Raman peak shifts relative to the LMC (Fig. 2*I*). The aragonitic outer skeleton contains ca. 1.2 mol% $SrCO_3$, with $MgCO_3$ below the electron microprobe detection limit, that is, similar to aragonitic skeletons of other deep-sea corals (15).

Both aragonitic and calcitic crystals have the *a* and *b* axis rotated around the *c* axis (turbostratic distribution) in the plane (222) of aragonite and ($10\bar{1}4$) of calcite (Fig. 2 *F–H*). Raman spectra in RADs and neighboring TD regions indicated disordered material in both calcite and aragonite RADs (Fig. 2 *I–K*). The aragonitic RADs showed stronger fluorescence than RADs in the calcitic inner skeleton (*SI Appendix*, Fig. S9 *A* and *B*).

The measured average $^{44}Ca/^{40}Ca$ isotope ratios of the aragonitic and calcitic skeletal parts were $-1.51 \pm 0.21‰$ and $-1.24 \pm 0.14‰$ (relative to seawater, 2σ). The mean $\delta^{44/40}Ca$ value of the inner calcitic skeleton is consistent with that observed in other biomineralizers that form HMC and have sophisticated control over biomineralization. The average $\delta^{44/40}Ca$ value of the aragonitic outer skeleton is consistent with other biogenic aragonites. The difference in the average oxygen isotopic composition between the calcitic inner and the aragonitic outer skeletons is less than 1‰ (*SI Appendix*, Fig. S15).

All these unique skeletal features of the *P. antarcticus* point to a distinct position of this taxon in the phylogeny of Scleractinia. To investigate this, we performed a mitophylogenomic analysis that involved all mitochondrial protein-encoding genes of *P. antarcticus* aligned to those from 57 other scleractinians and 12 corallimorpharians, the latter used as an outgroup (*SI Appendix*, Table S2). The resulting phylogeny placed *P. antarcticus* in an early diverging position within the Vacatina (Robusta) clade, with time calibration indicating a Cretaceous (ca. 116 Ma) divergence of its lineage (Fig. 3).

Discussion

Although calcitic deposits can be observed in adult skeletons of modern scleractinians, these are invariably considered to be secondary calicite cements or products of calcite precipitation induced by other organisms, such as skeletal borers and/or microbes (16, 17). The occurrence of HMC in *P. antarcticus* skeleton was noted previously (18) but interpreted as diagenetic infilling of microborer cavities. It is, however, highly unlikely that the calcitic inner skeleton of *P. antarcticus* is the result of alteration by the postformation processes for a number of reasons. 1) The examined skeletons of *P. antarcticus* exhibit no signs of borings. Other corals collected alive from the same localities at the same time (e.g., *Flabellum flexuosum* and *Javania antarctica*) show no signs of calcite or other diagenetic alteration (*SI Appendix*, Figs. S11 and S12). 2) The calcitic inner skeleton of *P. antarcticus* shows microstructural components typical of scleractinian corals with regularly arranged axial RADs and associated TD fibers. Diagenetic alteration of orthorhombic aragonite to hexagonal LMC is fabric destructive. Furthermore, neomorphism from aragonite to HMC is very unlikely because HMC is more soluble and less stable. Metastable aragonite and HMC invariably neomorphose to more stable LMC (or dolomite). 3) The inner skeleton shows no trace of red luminescence (cathodoluminescence) typical of carbonates from diagenetic environments enriched with activator ions, such as Mn^{2+} (*SI Appendix*, Fig. S9). 4) The presence of disordered material in both calcitic and aragonitic RADs is revealed by Raman spectroscopy and is suggestive of putative protocalcite and protoaragonite, respectively (19). In combination with the nanoparticulate texture of all skeletal components (Fig. 2), this is consistent with a biogenic, nonclassical mineralization process

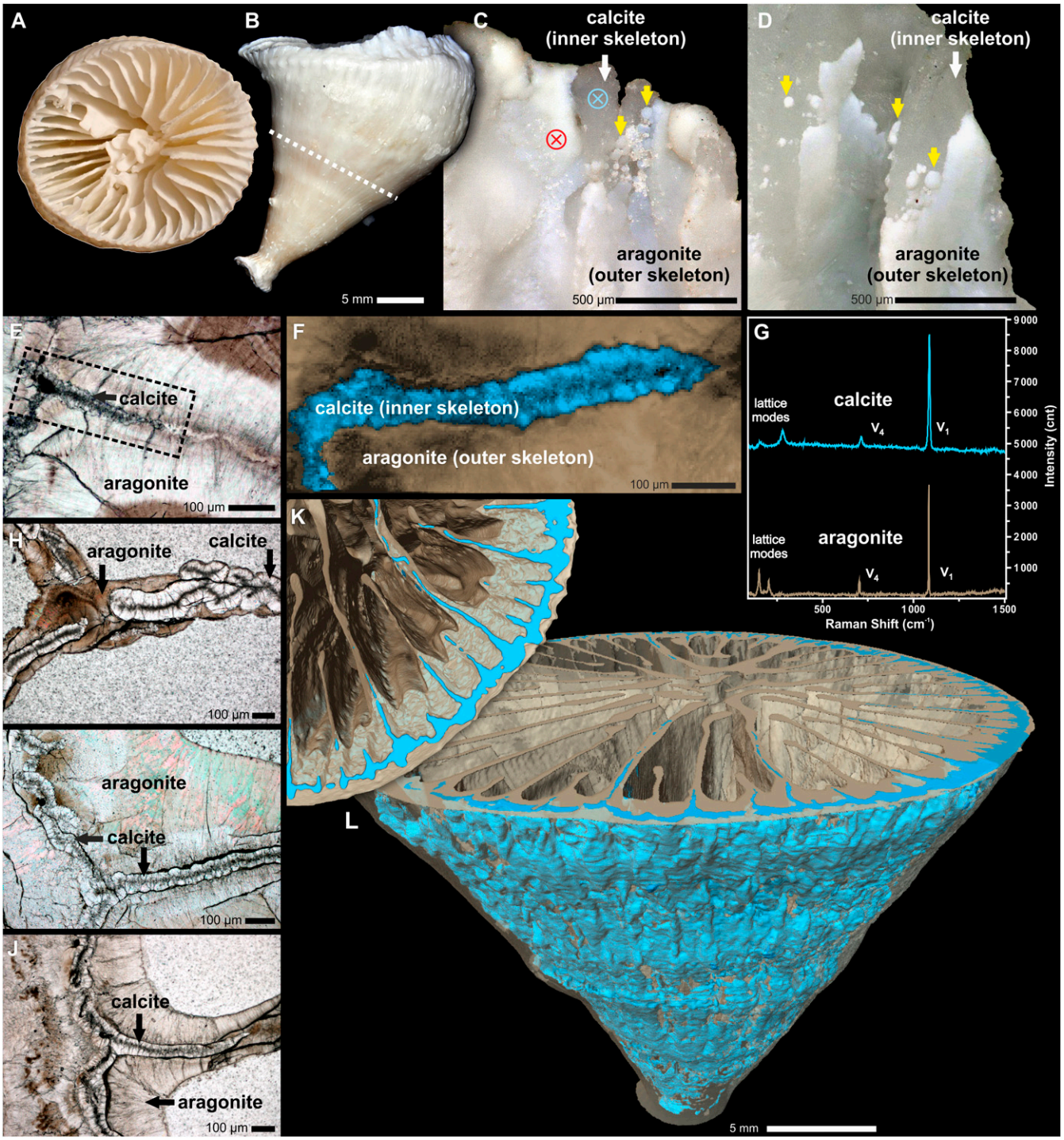

Fig. 1. Extant specimen of the solitary scleractinian coral *Paraconotrochus antarcticus* with a two-component calcitic (inner)–aragonitic (outer) skeleton. Distal (*A*) and lateral (*B*) views of the calice are shown. (*C* and *D*) The growth edges of the septa and wall exhibit a calcitic inner skeleton (white arrows) overgrown by an aragonite (outer) skeleton (yellow arrows); blue- and red-crossed circles mark the position of micro-Raman analyses. (*F*) A Raman map (region marked in *E*) showing the distribution of calcite (blue) and aragonite (beige) in a skeleton sectioned transversely. (*G*) Raman spectra (from 0 to 1,500 cm^{-1} that include both lattice and internal [v1, v4], vibrational modes) of coral aragonite (beige) and calcite (blue) collected from regions indicated in *C*. (*H–J*) Transverse sections of adult (*H*), juvenile (*I*), and early juvenile (*J*) parts of the calice. Distinct boundaries (i.e., heteroepitaxy) between the crystal-transparent calcitic regions (with dark RADs) and the brownish aragonitic regions are visible. (*K* and *L*) X-ray computed tomography visualization of the calcitic inner (blue) and the aragonitic outer skeleton (semitransparent beige) up to the level indicated with a dashed line in *B*. (*A–C*, *E*, and *G*) ZPAL H.25/114; (*D*) ZPAL H.25/115; (*E* and *F*) ZPAL H.25/116; (*H*, *I*, and *J*) ZPAL H.25/117.

with a continuous assemblage of amorphous intermediate precursors (i.e., amorphous calcium carbonate [ACC]) (14, 20–23). If a diagenetic process had transformed ACC into calcite and aragonite postmortem, that is, in the absence of a continued biomineralization process, the difference in molar volume between the ACC (ca. 54 cm^3/mol) and calcite or aragonite (both

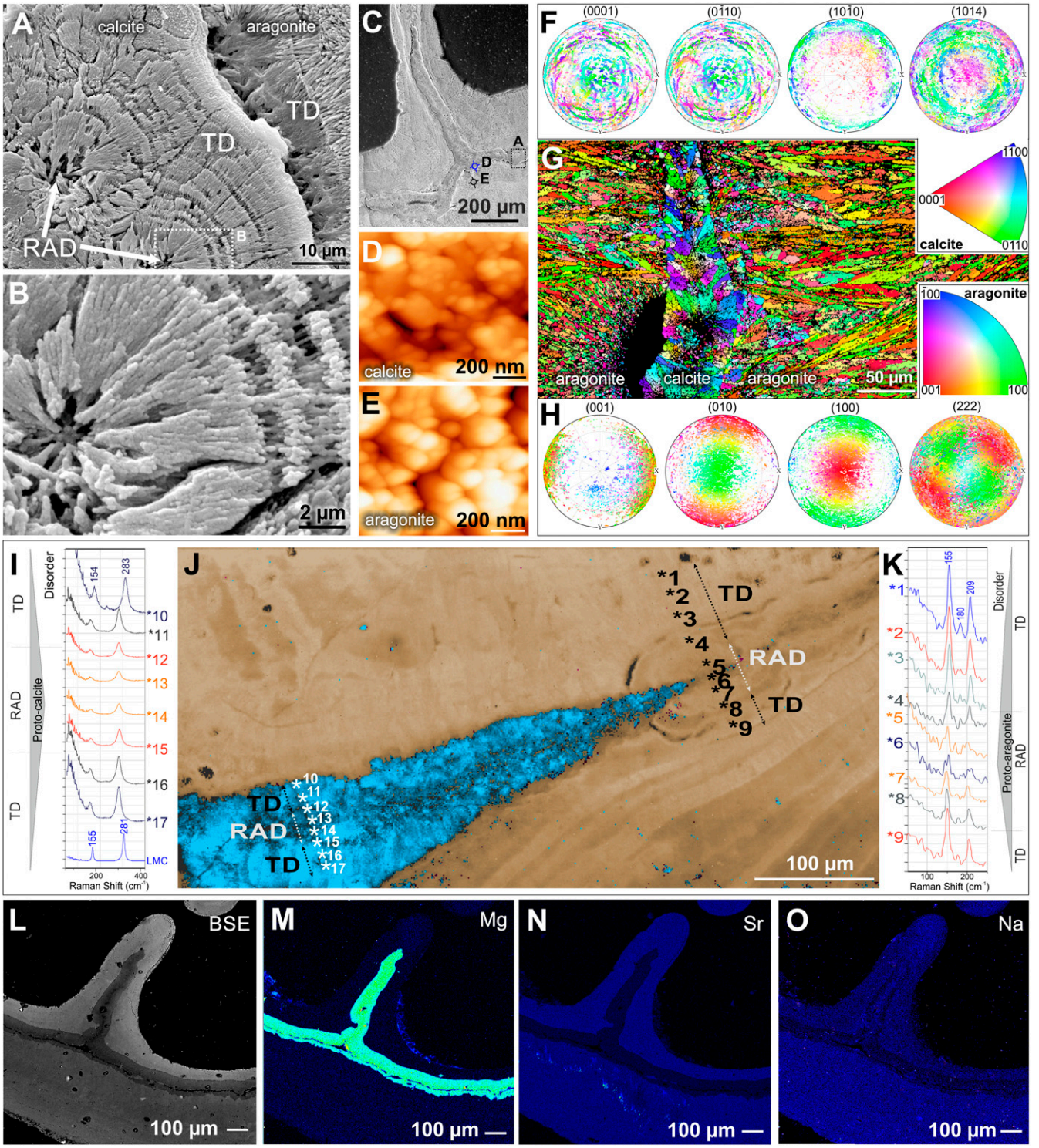

Fig. 2. The microstructural, crystallographic, and geochemical features of calcitic and aragonitic regions of *Paraconotrochus antarcticus* skeleton. (*A* and *B*) The calcitic inner skeleton consists of RADs (arrows) and fibrous layers (i.e., TDs). (*C*–*E*) SEM of a transversely sectioned skeleton with a dashed frame indicating the region enlarged in *A*, whereas blue (*D*) and black (*E*) circles mark areas observed by AFM. Both calcitic (*D*) and aragonitic (*E*) skeletal parts have a nanogranular texture, typical of biominerals. (*F*–*H*) The sharp crystallographic boundary between the inner calcitic and outer aragonitic skeleton (*G*); in both regions, crystals have their *a* and *b* axes rotating around a *c* axis (turbostratic distribution: calcite (*F*) in the plane 10$\bar{1}$4 and aragonite (*H*) in the plane 222. (*I*–*K*) The Raman spectra in RADs and neighboring TD regions (numbers in *J* mark measurement points) indicate disordered material in both calcite (*I*) and aragonite RADs (*K*), consistent with biogenic formation from amorphous precursors. (*J*) A Raman map. (*L*–*O*) Back-scattered electron (BSE) and electron microprobe images show the expected contrasting trace-element distributions, with calcite enriched in Mg (*M*) and depleted in Sr (*N*) and Na (*O*) compared with aragonite. (*A*–*E* and *L*–*O*) ZPAL H.25/117; (*F*–*K*) ZPAL H.25/116.

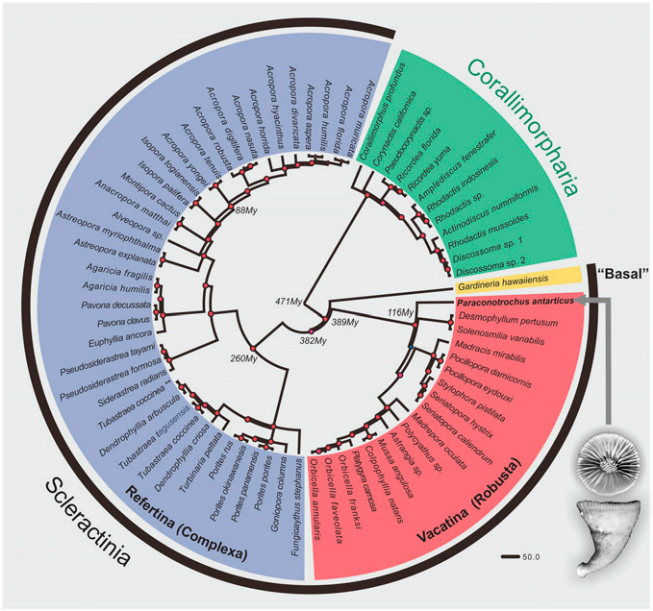

Fig. 3. The position of *Paraconotrochus antarcticus* (arrow) in phylogeny of the scleractinia. The early-diverging *Gardineria hawaiiensis* ("Basal"), the Vacatina (Robusta), and Refertina (Complexa) are shown. *P. antarcticus* has an early-diverging position within the Vacatina clade, from which it diverged in the Mesozoic (Cretaceous) ca. 116 Ma. The diagram is based on maximum likelihood (ML) and Bayesian inference of concatenated nucleotides from all mitochondrial protein-coding genes. Small red circles on nodes indicate ML and posterior probability support of 100 and 1, respectively. The numbers close to some nodes indicate estimated divergence times using a relaxed molecular clock (uncorrelated log-normal).

ca. 37 cm^3/mol) would result in clearly visible porosity, which was not observed. 5) A primary origin of the *P. antarcticus* skeleton is also supported by the crystallographic arrangement of aragonitic and calcitic crystals that have *a* and *b* axes rotated around the *c* axis (turbostratic distribution), which is considered to be a biogenic strategy to prevent crystal cleavage (Fig. 2) (24). 6) The distalmost edge of the septa, which represents the growth-edge, and hence the most recently formed skeleton, exhibits the same calcitic component as septal regions deeper in the calice (inner skeleton). If the inner skeleton is the result of a transformation from aragonite, or another precursor (for example, ACC), this transformation must be nearly instantaneous.

A primary biogenic origin of the inner calcitic skeleton is also supported by its stable isotopic compositions. The measured average $^{44}Ca/^{40}Ca$ isotope ratios of the aragonitic and calcitic skeletal parts are consistent with the values observed for biocalcifiers with skeletons of similar mineralogy and recognized to exert strong control over their biomineralization process (25, 26) (*SI Appendix*, Figs. S13 and S14 and Table S3). In addition, low Sr/Ca and high Mg/Ca ratios indicate that the calcite $\delta^{44/40}Ca$ did not result from closed-system diagenetic recrystallization of aragonite to calcite (27, 28). Open-system diagenetic recrystallization would have shifted calcium isotope ratios to much higher values ($\delta^{44/40}Ca > -1‰$) (*SI Appendix*, Fig. S13). The average oxygen isotopic composition between the calcitic inner and the aragonitic outer skeletons is less than 1‰, which is consistent with observations of, for example, bimineralic bivalves (29). Furthermore, the oxygen isotopic variability observed at the micrometer scale in the inner- and outer-skeletal parts is similar to that observed in other coral skeletons (30, 31) and can only be ascribed to vital effects (*SI Appendix*, Figs. S15 and S16 and Table S4) (15, 30). We thus conclude that the inner calcitic skeleton in *P. antarcticus* is pristine and the result of a highly controlled biomineralization mechanism as opposed to secondary alteration.

The evolutionary stability of skeletal mineralogy and biomineralization patterns of scleractinian corals is now widely recognized (32). With regard to *Paraconotrochus* and *Coelosmilia*, this implies that they may very well have had a common evolutionary history. The mitophylogenomic analysis indicated a Cretaceous (ca. 116 Ma) divergence of its lineage (Fig. 3), coinciding with the lowest ocean Mg/Ca ratio during the Phanerozoic (<1 mol/mol). Culturing experiments have suggested that low-Mg seawater chemistry strongly affects the expression of genes related to coral skeletal formation and may trigger a change from aragonite to calcite mineralogy (33). Other experiments have demonstrated a physiologically controlled calcite-to-aragonite mineralogical switch triggered by changes in the growth solution Mg/Ca ratio (21, 34, 35). Although the majority of coral lineages that survived through the major changes in the oceanic Mg/Ca ratio continued to produce aragonitic skeletons, Cretaceous *Coelosmilia* was capable of developing a purely calcitic corallum (9). *P. antarcticus*, which has skeletal morphology and microstructure very similar to *Coelosmilia* (*SI Appendix*, Fig. S1), may be a direct descendant of this (or another) Mesozoic coral lineage capable of depositing a calcitic skeleton.

Conclusions and Perspective

This discovery of a two-component calcite–aragonite skeleton produced by extant *P. antarcticus* offers an opportunity to greatly enhance the understanding of the scleractinian biomineralization process, which, necessarily, is highly controlled by the animal. It also provides a unique window into the evolutionary history of scleractinian corals and changes the basis for theories about scleractinian coral evolution through geological time (during which ocean chemistry varied substantially to favor either aragonite or calcite production) by removing the obstacle that skeletal mineralogy defines an impassable boundary between higher level anthozoan taxonomic units.

Despite dramatic physicochemical changes of the marine environment(s) surrounding the Antarctic continent since the Mesozoic (36), the Southern Ocean is recognized as an evolutionary refuge for numerous benthic invertebrates. Among these, about 30 modern Southern Ocean molluscan genera already existed in the late Cretaceous–early Paleogene (37). The long-term survival of these benthic metazoans in the Southern Ocean can be ascribed to its relative isolation and unique environmental conditions over the last 100 Myr (38). The presence of early-diverging *P. antarcticus* in the Southern Ocean suggests that this region has also played an important role as refuge for the evolution of asymbiotic scleractinian corals. The corals living there may carry the answer to a series of fundamental evolutionary questions: what are the genetic and/or environmental underpinnings of the calcite-forming capability in corals? Is the *Paraconotrochus* the only living scleractinian capable of calcite skeleton formation? Was there a higher diversity of such corals in the geological past? Is the mineralogical difference still to be considered a major obstacle for evolutionary transition between Paleozoic rugosan and scleractinian corals (39)?

Today, anthropogenic climate change and ocean acidification is rapidly impacting the polar regions. High-latitude seawater is predicted to become undersaturated with respect to aragonite and high-Mg calcite within a few decades because of ocean uptake of anthropogenic CO_2. Such changes represent an existential threat to marine calcifying organisms (40, 41) endemic to these regions. The observations presented here further emphasize the uniqueness of the Southern Ocean as a repository for ancient traits and an important window into the evolutionary history of marine benthic organisms. We have much more to learn from these environments and their inhabitants, which further enhances the need for their preservation.

Materials and Methods

Materials. Detailed information about the examined material is provided in the *SI Appendix, SI Materials*. This study is based on the examination of a large collection of *P. antarcticus* from three major regions of the Southern Ocean (Weddell Sea, Ross Sea, and Cooperation Sea). In addition to the specimens housed as dry skeletons, we also examined skeletons of *P. antarcticus* collected alive in Weddell Sea and Cooperation Sea and preserved in 70% ethanol. Because of their excellent preservation condition, molecular analysis of specimens collected alive by the RRS James Clark Ross (British Antarctic Survey) off Antarctica in March 2016 was possible.

Methods: Skeletal Analyses.

Atomic Force Microscopy. The AFM allows for the determination of the 3D surface topology of the biomineral at nanometer resolution. Following established procedures (42), measurements were performed using the Multimode 5 Atomic Force Microscopy instrument (Veeco) upgraded to Multimode 8 version (Bruker). The images have been acquired in ScanAsyst mode.

Cathodoluminescence microscopy. Cathodoluminescence microscopy is a method to determine the spatial distribution of primary and secondary features of carbonate samples. Diagenetic environments enriched with activator ions such as Mn are usually reducing (low Eh). Secondary calcite that was altered within a reducing diagenetic environment—in contrast to original carbonate skeleton—typically contains a high concentration of Mn^{2+} (the main activator of luminescence in carbonates) and exhibits strong orange to red luminescence. Cathodoluminescence of the thin-sectioned skeleton of *P. antarcticus* was examined with a hot cathode microscope HC1-LM at the Institute of Paleobiology, Polish Academy of Sciences, operated with an electron energy of 14 keV and a beam current density of 0.1 $\mu A/mm^{-2}$.

Confocal laser scanning microcopy. Confocal laser scanning microcopy (CLSM) is a type of high-resolution fluorescence microscopy that facilitates the generation of high-resolution images from relatively thick sections. CLSM observations were conducted on sectioned skeletons of *P. antarcticus* using a Nikon Eclipse Ti inverted fluorescence microscope from the Laboratory of Electron and Confocal Microscopy at the Faculty of Biology (University of Warsaw) equipped with 488 nm lasers; a 32-channel spectral detector with a resolution of 2, 5, 6, or 10 nm; and mode Virtual Filter linked to Nikon's DS-5Mc video camera with charged-coupled device detector with a resolution of 5 Mpx.

Electron microprobe analysis. The electron microprobe analysis mapping enables simultaneous analysis of different elements and the generation of distribution maps for each element with ca. 1-μm lateral resolution. The measurements were conducted on polished and C-coated thin sections with a JEOL Superprobe JZA-8900 equipped with five wavelength-dispersive spectrometers at the National Centre of Electron Microscopy (the Universidad Complutense of Madrid, Spain). Four elements (Ca, Mg, Sr, and Na) were mapped (800 × 800 points) (Fig. 2 *K–M*). An accelerating voltage of 20 kV with a beam current of 50 nA and a spot size and step interval of 1 μm in diameter (dwell time = 20 ms) were used.

Electron backscatter diffraction. The electron backscatter diffraction (EBSD) is a scanning electron microscope–based microstructural–crystallographic characterization technique that can provide information about, for example, the phase and crystal orientation in the material. Thin-sectioned samples were polished with alumina of 9 μm, 1 μm, and 0.3 μm and then with colloidal silica (0.05 μm). Before analysis, samples were cleaned, dried, and coated with a conducting carbon layer ca. 3 nm in thickness using a BALTEC SCD 005 sputter coater. The EBSD study was carried out with an Oxford NordlysMax detector mounted on a scanning electron microscope JEOL JSM-6610LV at the Institute of Materials Engineering, Łódź University of Technology. EBSD data were collected with AztecHKL software at high vacuum, 20 kV, large probe current, and 20 mm of working distance. EBSD patterns were collected at a resolution of 0.22 μm step size for crystallographic maps using the unit cell settings characteristic of aragonite and calcite as follows: "Pmcn" symmetry and a = 4.96 Å, b = 7.97 Å, and c = 5.75 Å estimated for *Favia* coral using X-ray powder diffraction with synchrotron radiation (43) and a = b = 4.99 Å, and c = 17.06 Å, respectively. EBSD data were processed using CHANNEL 5 software from Oxford Instruments. The EBSD data are represented as phase maps (showing the distribution of the different mineral phases), band contrast images (showing the quality of the material diffraction), and color-coded crystallographic orientation images with corresponding pole figures of aragonite and calcite in selected regions. The MATLAB toolbox MTEX (44) was used for the stereographic projection of crystallographic planes in reference to the (001), (010), (100), and (222) for aragonite and (0001), $(01\bar{1}0)$, $(10\bar{1}0)$, and $(10\bar{1}4)$ for calcite.

Feigl's solution chemical staining. This staining technique allows us to distinguish aragonite from other calcium carbonate polymorphs. The Feigl's method is based on slightly different dissolution rates of calcite and aragonite in water, and the larger reactive surface of fine-crystalline aragonite regions results in their intense black staining. Accordingly, aragonite regions were darkly stained, whereas calcite remained uncolored. The surfaces of coral skeletons were polished with an aluminum oxide suspension with a 0.25-μm particle size and rinsed with distilled water. The specimens were next immersed in several milliliters of Feigls's solution (45) and stained for 10 to 15 min.

Isotope analyses (calcium isotopes). Calcium isotope preparation and analyses were performed at Princeton University. The specimen was microdrilled using a Brasseler scriber point carbide drill bit (H1621.11.008 HP) on an ESI MicroMill. The smallest available drill diameter (~100 μm) was used to drill precisely in the inner calcite skeleton and minimize introduction of the outer skeleton aragonite. Microdrilled carbonate was dissolved directly in 0.2% nitric acid for chromatography. Calcium was isolated from matrix elements on an automated Dionex ICS-5000+ ion chromatography system coupled with a Dionex AS-AP fraction collector using previously published methods (26, 27, 46, 47). Following ion separation, samples were treated with concentrated HNO_3 and then dried and rediluted in 2% HNO_3 for mass spectrometry.

Calcium isotope ratios were measured on a Thermo Scientific Neptune Plus multicollector inductively coupled plasma mass spectrometer (MC-ICP-MS). Sample solution concentrations were carefully matched to a standard solution concentration of 2 ppm Ca to minimize concentration-dependent isotope effects. The analyses were performed with an ESI Apex-IR sample introduction system using medium resolution mode to avoid isobaric $^{87}Sr^{2+}$ and $ArHH^+$ interferences. Measured $\delta^{44/42}Ca$ values were converted (48) to $\delta^{44/40}Ca$ values assuming a mass-dependent fractionation with a slope of 2.05 and assuming no excess radiogenic ^{40}Ca. All Ca isotope values were plotted in 3-isotope space ($\delta^{44/42}Ca$ versus $\delta^{43/42}Ca$) to verify that the Ca isotopes fall along the expected mass-dependent line.

All data are reported in delta notation relative to modern seawater ($\delta^{44/40}Ca_{seawater}$ = 0‰). $\delta^{44/40}Ca_{seawater}$ = +1.92‰ on the Standard Reference Material 915a (SRM915a) scale and +0.98‰ on the bulk silicate Earth scale (48). We report long-term external reproducibility using the measured value of SRM915b relative to modern seawater, both of which are taken through the full chemical procedure (column chromatography and mass spectrometry) with each batch of samples. Our measured $\delta^{44/40}Ca$ value for SRM915b relative to modern seawater is -1.22 ± 0.14‰ (2σ; $n = 39$), indistinguishable from published values determined by both MC-ICP-MS and thermal ionization mass spectrometry (TIMS) (48, 49).

Isotope analyses (oxygen isotopes). Oxygen isotope ratios were measured by secondary ion mass spectrometry (SIMS) using the CAMECA IMS 1280-HR at the SwissSIMS laboratory (University of Lausanne, Switzerland). A focused high-density Cs^+ primary beam (Gaussian mode, 1.3 nA) at 10 kV was used to analyze oxygen isotope ratios. The spot size was 10 to 15 μm, and no raster was used. $^{16}O^-$ and $^{18}O^-$ were collected simultaneously on Faraday cups with a mass resolution of ca. 2200. The electron flood gun, with normal incidence, was used to compensate charges. Mass calibration was performed at the beginning of the session. Each analysis took ~4 min, including presputtering (30 s) and automated centering of secondary electrons. Each data point consisted of 10 measurements; the error of the mean was always better than 0.3‰ (2 SDs). Instrumental mass-fractionation was determined using a calcite and an aragonite standard, mounted together with the sample. Because the Mg content of carbonate affects the instrumental mass fractionation, the $\delta^{18}O$ value of the high-Mg calcite was corrected using the calibration of Rollion-Bard and Marin-Carbonne (50). The reproducibility of the calcite standard was 0.38‰ (2 SDs), and the reproducibility of the aragonite standard was 0.23‰ (2 SDs) over the session. No drift correction was applied. $\delta^{18}O$ is referenced to the standard mean ocean water Pee Dee Belemnite (PDB) $^{18}O/^{16}O$ ratio of $2{,}005.2 \times 10^{-6}$.

Optical microscopy. Polished sections were examined using a Nikon Eclipse 80i transmitted light microscope fitted with a DS-5Mc cooled camera head. Observations were conducted in transmitted and polarized light. The micromorphological details of calcite–aragonite contact at distal parts of the septa and wall were examined by the Keyence VHX-5000 Digital Microscope at the Institute of Paleobiology, Warsaw, Poland (the help of Łucja Fostowicz-Frelik is greatly appreciated).

Raman microscope. The Raman measurements were performed with LabRAM 800 HR confocal microscope (Horiba Jobin Yvon) equipped with a diode-pumped Nd:YAG laser (Spectra-Physics) operating at 532.3 nm (ca. 2 mW power on the sample). The individual spectra were recorded using 1,800 groove/mm holographic grating, while for the acquisition of maps, the

600-groove/mm grating was used. The most convenient signals allowing for identification of the calcite and aragonite polymorphs are grouped in the 100 cm^{-1} to 300 cm^{-1} region. These peaks, associated with lattice vibrations, appear at 205 cm^{-1} and 153 cm^{-1} for aragonite and at 281 cm^{-1} and 153 cm^{-1} for calcite. The analysis of the maps was performed employing the modeling option of the Labspec software (Horiba Jobin Yvon).

SEM. Polished sections were lightly etched in Mutvei's solution following described procedures (51) and then rinsed with Milli-Q water and air-dried. After drying, the specimens were put on stubs with double-sticking tape and sputter-coated with conductive platinum film. Analyses were made using a Phillips XL20 scanning electron microscope at the Institute of Paleobiology, Warsaw, Poland.

X-ray microtomography. The density difference between inner calcitic and outer aragonitic skeleton [in theory, 2.71 g/cm^{-3} versus 2.93 g/cm^{-3}, but slightly lower in biominerals that contain organic inclusions (52)] makes these skeletal regions distinguishable with high-resolution 3D tomography. Micro computed tomography data were collected with Zeiss XRadia MicroXCT-400 system at the Faculty of Materials Science and Engineering, Warsaw University of Technology system. Scans of a lower portion of ZPAL H.25/114 specimen of *P. antarcticus* were performed using the following parameters: voltage: 80 kV, power: 10 W, exposure time: 3 s, pixel size: 19.26 μm, 1,000 projections. Radial projections were reconstructed with XMReconstructor software provided with the Zeiss Xradia system. The 3D images of calcitic inner and aragonitic outer skeleton were obtained by processing with the AVIZO7.1 Fire Edition software.

Methods: Molecular and Phylogenetic Analyses. *P. antarcticus* total genomic DNA was extracted following a modified cetyltrimethylammonium bromide (CTAB) protocol (53) with an additional cleanup step using the Qiagen Power Clean Kit. Extracted DNA quality and yield were assessed and measured on a 1% agarose gel and Qubit 2.0 fluorometer, respectively. Library preparation, target enrichment of ultraconserved elements and exons, and sequencing details followed those provided in Quattrini et al. (54).

Resulting sequences were assembled using Spades 3.10 (55), and the mitogenome was annotated in MITOS2 (56) and Geneious R10.2.3 (57). The *P. antarcticus* mitogenome was aligned using MAFFT version 7 (58) to 57 other scleractinians and 12 corallimorpharians previously published mitogenomes, of which corallimorpharians were used as the outgroth (*SI Appendix*, Table S2). The final alignment consisted of 10,860 bp and contained the nucleotide sequences from all mitochondrial protein coding genes. Mitophylogenomic Maximum Likelihood (ML) analyses were based on approximate likelihood ratio test using PhyML 3.0 (59) and 100 bootstrap replicates using RAxML (60) implemented at CIPRES (61) under the General Time Reversible (GTR) + G + I model of nucleotide substitution. Bayesian inference was performed on MrBayes also implemented at CIPRES with two runs each containing 100,000 generations saved at every 1,000, with a burn-in factor of 0.25. Uncorrelated relaxed molecular clock with a log-normal distribution was run on BEAST2 (62) under the Yule speciation process (63) and calibrated using the following time points: *Acropora*, 55 My; Dendrophylliidae, 127 My; Poritidae/Dendrophylliidae, 130 My; Agariciidae, 220 My; and Pocilloporidae, 70 My. Normal distribution was selected for each calibration point with an SD of 10%. For this analysis, the same model of nucleotide substitution was used in two separated runs, each with 10,000,000 generations saved every 10,000. The first 300 generations from each run were discarded as burn-in, and the remaining generations from each run were combined using LogCombiner version 1.10.4. The root from the recovered topology/molecular clock estimates was scaled to 470 My.

Data Availability. Mitogenome sequences data have been deposited in GenBank (MT409109). All other study data are included in the article text and supporting information.

ACKNOWLEDGMENTS. This work was funded in part by the National Science Centre (Poland) research grant 2017/25/B/ST10/02221 to J.S. and by a European Research Council Advanced Grant number 788752 (UltraPal) to A.M. M.V.K. is supported by the São Paulo Research Foundation (Fundação de Amparo à Pesquisa do Estado de São Paulo 2014/01332-0 and 2017/50229-5) and National Science Council (Conselho Nacional de Desenvolvimento Científico e Tecnológico 301436/2018-5). L.F.R. and M.L.T. were supported by the UK Natural Environment Research Council NE/R005117/1. The RRS James Clark Ross JR15005 cruise was part of the Biodiversity, Evolution, and Adaptation team of the Environmental Change and Evolution Programme at British Antarctic Survey. Funding of the mitogenome of *P. antarcticus* was provided by the NSF (1457817 to C.S.M. and 1457581 to E. Rodriguez). The work was also partially supported by the European Union within the European Regional Development Fund, through the Innovative Economy Operational Program POIG.02.02.00-00-025/09 (NanoFun).

1. R. Wood, A. Y. Ivantsov, A. Y. Zhuravlev, First macrobiota biomineralization was environmentally triggered. *Proc. Biol. Sci.* **284**, 20170059 (2017).
2. R. Wood, *Reef Evolution* (Oxford University Press, Oxford, New York, 1999).
3. G. Falini, S. Fermani, S. Goffredo, Coral biomineralization: A focus on intra-skeletal organic matrix and calcification. *Semin. Cell Dev. Biol.* **46**, 17–26 (2015).
4. J. W. Morse, Q. Wang, M. Y. Tsio, Influences of temperature and Mg:Ca ratio on CaCO3 precipitates from seawater. *Geology* **25**, 85–87 (1997).
5. L. A. Hardie, Secular variation in seawater chemistry: An explanation for the coupled secular variation in the mineralogies of marine limestones and potash evaporites over the past 600 m.y. *Geology* **24**, 279–283 (1996).
6. P. Bots, L. G. Benning, R. E. M. Rickaby, S. Shaw, The role of SO4 in the switch from calcite to aragonite seas. *Geology* **39**, 331–334 (2011).
7. S. M. Stanley, L. A. Hardie, Secular oscillations in the carbonate mineralogy of reef-building and sediment-producing organisms driven by tectonically forced shifts in seawater chemistry. *Palaeogeogr. Palaeoclimatol. Palaeoecol.* **144**, 3–19 (1998).
8. U. Balthasar, M. Cusack, Aragonite-calcite seas—Quantifying the gray area. *Geology* **43**, 99–102 (2015).
9. J. Stolarski, A. Meibom, R. Przenioslo, M. Mazur, A Cretaceous scleractinian coral with a calcitic skeleton. *Science* **318**, 92–94 (2007).
10. J. Stolarski *et al.*, The ancient evolutionary origins of Scleractinia revealed by azooxanthellate corals. *BMC Evol. Biol.* **11**, 316 (2011).
11. J. Stolarski *et al.*, A unique coral biomineralization pattern has resisted 40 million years of major ocean chemistry change. *Sci. Rep.* **6**, 27579 (2016).
12. K. Janiszewska, M. Mazur, S. Escrig, A. Meibom, J. Stolarski, Aragonitic scleractinian corals in the Cretaceous calcitic sea. *Geology* **45**, 319–322 (2017).
13. S. D. Cairns, Antarctic and subantarctic Scleractinia. *Antarct. Res. Ser.* **34**, 1–74 (1982).
14. P. U. P. A. Gilbert *et al.*, Biomineralization by particle attachment in early animals. *Proc. Natl. Acad. Sci. U.S.A.* **116**, 17659–17665 (2019).
15. A. Meibom *et al.*, Compositional variations at ultra-structure length scales in coral skeleton. *Geochim. Cosmochim. Acta* **72**, 1555–1569 (2008).
16. L. D. Nothdurft, G. E. Webb, T. Bostrom, L. Rintoul, Calcite-filled borings in the most recently deposited skeleton in live-collected Porites (Scleractinia): Implications for trace element archives. *Geochim. Cosmochim. Acta* **71**, 5423–5438 (2007).
17. P. Dalbeck *et al.*, Identification and composition of secondary meniscus calcite in fossil coral and the effect on predicted sea surface temperature. *Chem. Geol.* **280**, 314–322 (2011).
18. K. Cuny-Guirriec *et al.*, Coral Li/Mg thermometry: Caveats and constraints. *Chem. Geol.* **523**, 162–178 (2019).
19. O. Sibony-Nevo *et al.*, The pteropod Creseis acicula forms its shell through a disordered nascent aragonite phase. *Cryst. Growth Des.* **19**, 2564–2573 (2019).
20. S. Von Euw *et al.*, Biological control of aragonite formation in stony corals. *Science* **356**, 933–938 (2017).
21. T. Mass *et al.*, Amorphous calcium carbonate particles form coral skeletons. *Proc. Natl. Acad. Sci. U.S.A.* **114**, E7670–E7678 (2017).
22. X. Long, Y. Ma, L. Qi, Biogenic and synthetic high magnesium calcite–A review. *J. Struct. Biol.* **185**, 1–14 (2014).
23. S. Weiner, I. Sagi, L. Addadi, Structural biology. Choosing the crystallization path less traveled. *Science* **309**, 1027–1028 (2005).
24. I. Coronado, A. Pérez-Huerta, S. Rodríguez, G. Sevastopulo, Crystallographic orientations of structural elements in skeletons of syringoporicae (tabulate corals, Carboniferous): Implications for biomineralization processes in palaeozoic corals. *Palaeontology* **58**, 111–132 (2015).
25. N. Gussone *et al.*, *Calcium Stable Isotope Geochemistry: Advances in Isotope Geochemistry* (Springer-Verlag Berlin Heidelberg, 2016).
26. C. L. Blättler, G. M. Henderson, H. C. Jenkyns, Explaining the Phanerozoic Ca isotope history of seawater. *Geology* **40**, 843–846 (2012).
27. J. A. Higgins *et al.*, Mineralogy, early marine diagenesis, and the chemistry of shallow-water carbonate sediments. *Geochim. Cosmochim. Acta* **220**, 512–534 (2018).
28. T. Steuber, D. Buhl, Calcium-isotope fractionation in selected modern and ancient marine carbonates. *Geochim. Cosmochim. Acta* **70**, 5507–5521 (2006).
29. C. Lécuyer *et al.*, Carbon and oxygen isotope fractionations between aragonite and calcite of shells from modern molluscs. *Chem. Geol.* **332–333**, 92–101 (2012).
30. A. Meibom *et al.*, Vital effects in coral skeletal composition display strict three-dimensional control. *Geophys. Res. Lett.* **33**, L11608 (2006).
31. N. Allison, A. A. Finch, The potential origins and palaeoenvironmental implications of high temporal resolution δ18O heterogeneity in coral skeletons. *Geochim. Cosmochim. Acta* **74**, 5537–5548 (2010).
32. J. L. Drake *et al.*, How corals made rocks through the ages. *Glob. Change Biol.* **26**, 31–53 (2020).
33. I. Yuyama, T. Higuchi, Differential gene expression in skeletal organic matrix proteins of scleractinian corals associated with mixed aragonite/calcite skeletons under low *m*Mg/Ca conditions. *PeerJ* **7**, e7241 (2019).
34. A. Akiva *et al.*, Minerals in the pre-settled coral Stylophora pistillata crystallize via protein and ion changes. *Nat. Commun.* **9**, 1880 (2018).
35. R. Gavriel *et al.*, The coral protein CARP3 acts from a disordered mineral surface film to divert Aragonite crystallization in favor of Mg-calcite. *Adv. Funct. Mater.* **28**, 1707321 (2018).
36. A. Clarke, J. A. Crame, The origin of the Southern Ocean marine fauna. *Geol. Soc. Lond. Spec. Publ.* **47**, 253 (1989).

37. J. A. Crame *et al*., The early origin of the antarctic marine fauna and its evolutionary implications. *PLoS One* **9**, e114743 (2014).
38. A. D. Rogers *et al*., Antarctic futures: An assessment of climate-driven changes in ecosystem structure, function, and service provisioning in the Southern Ocean. *Annu. Rev. Mar. Sci.* **12**, 87–120 (2020).
39. W. A. Oliver, The relationship of the scleractinian corals to the rugose corals. *Paleobiology* **6**, 146–160 (2016).
40. A. J. Andersson, F. T. Mackenzie, N. R. Bates, Life on the margin: Implications of ocean acidification on Mg-calcite, high latitude and cold-water marine calcifiers. *Mar. Ecol. Prog. Ser.* **373**, 265–273 (2008).
41. D. K. A. Barnes, G. A. Tarling, Polar oceans in a changing climate. *Curr. Biol.* **27**, R454–R460 (2017).
42. J. Stolarski, M. Mazur, Nanostructure of biogenic versus abiogenic calcium carbonate crystals. *Acta Palaeontol. Pol.* **50**, 847–865 (2005).
43. J. Stolarski, R. Przeniosło, M. Mazur, M. Brunelli, High-resolution synchrotron radiation studies on natural and thermally annealed scleractinian coral biominerals. *J. Appl. Cryst.* **40**, 2–9 (2007).
44. F. Bachmann, R. Hielscher, H. Schaeben, Grain detection from 2d and 3d EBSD data–specification of the MTEX algorithm. *Ultramicroscopy* **111**, 1720–1733 (2011).
45. M. F. Gerald, Identification of carbonate minerals by staining methods. *SEPM J. Sediment. Res.* **29**, 87–97 (1959).
46. J. M. Husson, J. A. Higgins, A. C. Maloof, B. Schoene, Ca and Mg isotope constraints on the origin of Earth's deepest δ13C excursion. *Geochim. Cosmochim. Acta* **160**, 243–266 (2015).
47. A. M. Gothmann *et al*., Calcium isotopes in scleractinian fossil corals since the Mesozoic: Implications for vital effects and biomineralization through time. *Earth Planet. Sci. Lett.* **444**, 205–214 (2016).
48. M. S. Fantle, E. T. Tipper, Calcium isotopes in the global biogeochemical Ca cycle: Implications for development of a Ca isotope proxy. *Earth Sci. Rev.* **129**, 148–177 (2014).
49. A. Heuser, A. Eisenhauer, The Calcium Isotope Composition, (δ44/40Ca) of NIST SRM 915b and NIST SRM 1486. *Geostand. Geoanal. Res.* **32**, 311–315 (2008).
50. C. Rollion-Bard, J. Marin-Carbonne, Determination of SIMS matrix effects on oxygen isotopic compositions in carbonates. *J. Anal. At. Spectrom.* **26**, 1285–1289 (2011).
51. B. R. Schöne, E. Dunca, J. Fiebig, M. Pfeiffer, Mutvei's solution: An ideal agent for resolving microgrowth structures of biogenic carbonates. *Palaeogeogr. Palaeoclimatol. Palaeoecol.* **228**, 149–166 (2005).
52. D. E. Jacob, R. Wirth, O. B. A. Agbaje, O. Branson, S. M. Eggins, Planktic foraminifera form their shells via metastable carbonate phases. *Nat. Commun.* **8**, 1265 (2017).
53. M. A. Coffroth, H. R. Lasker, M. E. Diamond, J. A. Bruenn, E. Bermingham, DNA fingerprints of a gorgonian coral: A method for detecting clonal structure in a vegetative species. *Mar. Biol.* **114**, 317–325 (1992).
54. A. M. Quattrini *et al*., Universal target-enrichment baits for anthozoan (Cnidaria) phylogenomics: New approaches to long-standing problems. *Mol. Ecol. Resour.* **18**, 281–295 (2018).
55. A. Bankevich *et al*., SPAdes: A new genome assembly algorithm and its applications to single-cell sequencing. *J. Comput. Biol.* **19**, 455–477 (2012).
56. M. Bernt *et al*., MITOS: Improved de novo metazoan mitochondrial genome annotation. *Mol. Phylogenet. Evol.* **69**, 313–319 (2013).
57. M. Kearse *et al*., Geneious basic: An integrated and extendable desktop software platform for the organization and analysis of sequence data. *Bioinformatics* **28**, 1647–1649 (2012).
58. K. Katoh, J. Rozewicki, K. D. Yamada, MAFFT online service: Multiple sequence alignment, interactive sequence choice and visualization. *Brief. Bioinform.* **20**, 1160–1166 (2019).
59. S. Guindon *et al*., New algorithms and methods to estimate maximum-likelihood phylogenies: Assessing the performance of PhyML 3.0. *Syst. Biol.* **59**, 307–321 (2010).
60. A. Stamatakis, RAxML version 8: A tool for phylogenetic analysis and post-analysis of large phylogenies. *Bioinformatics* **30**, 1312–1313 (2014).
61. M. A. Miller, W. Pfeiffer, T. Schwartz, "Creating the CIPRES science gateway for inference of large phylogenetic trees" in *Proceedings of the Gateway Computing Environments Workshop (GCE) 14 Nov. 2010* (New Orleans, LA, 2010), pp. 1–8.
62. R. Bouckaert *et al*., BEAST 2: A software platform for bayesian evolutionary analysis. *PLOS Comput. Biol.* **10**, e1003537 (2014).
63. T. Gernhard, The conditioned reconstructed process. *J. Theor. Biol.* **253**, 769–778 (2008).